

Role of Fault Gouge during Interaction between Hydraulic Fracture and a Preexisting Fracture

Mighani, S.

Earth, Atmospheric and Planetary Sciences Department, Massachusetts Institute of Technology, Cambridge, Massachusetts, USA.

Lockner, D. A. and Kilgore, B. D.

U.S. Geological Survey, Menlo Park, California, USA.

Evans, B.

Earth, Atmospheric and Planetary Sciences Department, Massachusetts Institute of Technology, Cambridge, Massachusetts, USA.

Copyright 2018 ARMA, American Rock Mechanics Association

ABSTRACT: Enhanced reservoir connectivity generally requires maximizing the intersection between hydraulic fracture (HF) and preexisting underground natural fractures (NF), while having the hydraulic fracture continue to propagate across the natural fractures. Observations of downhole core samples suggest that these natural fractures are in fact veins filled with minerals such as calcite (Mighani et al., 2016). We study this interaction during the approach of a hydraulic fracture to a smooth saw-cut fracture under triaxial stress conditions. The specimen is Solnhofen limestone, a fine-grained ($<5 \mu\text{m}$ grain), low permeability ($<10 \text{ nD}$) carbonate. The differential stress (1-20 MPa) and inclination of the fault which determines the approach angle, θ (30, 60°) are the experimental variables. We conduct the experiments on both bare surface and gouge-filled fault surfaces. The gouge is a 1 mm thick crushed powder of Solnhofen limestone with $<106 \mu\text{m}$ grain size. During the hydraulic fracture, acoustic emissions (AE), inferred slip velocity, axial stress and pore pressure are recorded at a 5 MHz sampling rate.

The hydraulic fracture was able to cross the bare surface fault with small induced fault slip. The fault gouge increased the coefficient of friction significantly from 0.12 (bare, polished surface) to > 0.44 (gouged layer). However, the gouge-filled fault arrested the hydraulic fracture and generated a slip event with different characteristics: 1- The stress drop was larger while the generated AE signals had lower magnitude. 2- Slip velocity recorded by the vibrometer was of the same order of magnitude for the bare and gouge-filled faults, but the slip duration increased from 29 μsec for bare surface to $\sim 2.5 \text{ msec}$ (~ 90 times longer rise time) for the gouge-filled fault. The experiments suggest that the gouge-filled fault can accommodate much larger displacement while promoting slow slip on the fault which is harder to detect as AE signals. The observed long duration slip events are similar to the field observations of the long period and long duration (LPLD) events during the stimulation of clay-rich shale formations (Zoback et al., 2012). While the intrinsic low strength, high ductility, and unfavorably oriented natural fractures in shale formations are expected to reduce the occurrence of induced seismicity, our experiments suggest an additional mechanism for the observed LPLD events, i.e. the role of fault gouge. They also suggest that the microseismic detection techniques may under-predict the stimulated volume as the activation of natural gouge-filled fractures may proceed aseismically.

1. INTRODUCTION

Hydraulic fracture (HF) operations have been extensively used over the years to increase the productivity of low-permeability hydrocarbon reservoirs. The intersection of hydraulic fractures with present underground natural fractures is proven as a major factor in increasing the productivity of the shale gas reservoirs (Mayerhofer et al., 2010). Microseismic observations (Mayerhofer et al., 2010) and mined-back downhole samples from field operations (Warpinski and Teufel, 1987) support the importance of natural fractures and their activation during the operation. Understanding the necessary conditions for the activation of natural fractures, the expected slip magnitude and enhanced fluid transmissivity, and the impact of this slip on the

hydraulic fracture path is a key to understanding the role of hydraulic fracture in enhanced recovery operations.

There is a vast literature on the interaction between a hydraulic fracture and a frictional interface as a proxy to natural fracture. The experiments in the literature have been conducted on specimens such as Nugget sandstone, Indiana limestone, PMMA (Hanson et al., 1980), Coconino sandstone (Warpinski and Teufel, 1987), Colton sandstone (Gu et al., 2012), Wondabyne sandstone (Bunger et al., 2015). The HF experiments in larger cubic blocks with 30 cm-1m side size have been conducted on shale samples such as Devonian shale (Blanton, 1982 and 1986). The heterogeneous nature of shale gas rocks is well known to the rock mechanics experimentalists. Therefore, having a multitude of shale samples with identical properties for parametric lab

studies is quite impossible, set aside the difficulties in obtaining a reliably solid shale sample with lab specific sizes. So, we would like to select a homogenous rock which represents the shale gas rock behavior. So, the Young's modulus needs to be on the moderate side i.e. 20-40 GPa (Mighani et al., 2015). It needs to be fine-grained with grain size $<10\ \mu\text{m}$. In addition, it needs to have a nD range permeability, i.e. $<100\ \text{nD}$ (Tinni et al., 2012). Solnhofen limestone is a finely grained ($<5\ \mu\text{m}$ grain), low permeability ($<10\ \text{nD}$) carbonate with a Young's modulus of 41 GPa and Poisson's ratio of 0.28. Therefore, Solnhofen limestone was a natural candidate and a better representative compared to sandstones.

The hydraulic fracture experiments in the literature were generally conducted on frictional interfaces with bare surface as a proxy to natural fracture. However, the *in-*

situ natural fractures in shale formations are apparently not bare surface and contain inclusions (Gale and Holder, 2007; Mighani et al., 2016). They are present as discontinuities filled with minerals such as calcite (Figure 1) precipitated during the formation's depositional history. The main scientific objective in this report is to answer the following question: "How is our current lab understanding of the interaction problem modified by inserting fault inclusions, i.e. fault gouge?"

The coefficient of friction is first measured in sliding experiments and followed by a set of hydraulic fracture experiments. Using high acquisition rate recordings of acoustic emissions (AE), pore pressure, and stresses, the dynamic processes during this interaction are studied. The influence of fault gouge and the relation between the lab and field HF operations are discussed.

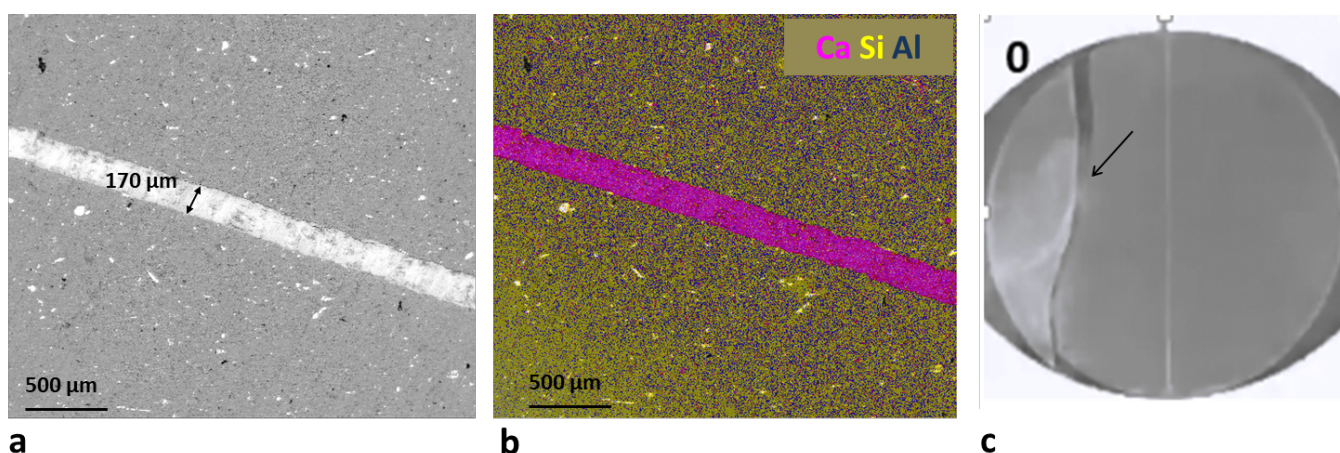


Figure 1. a) Backscattered SEM image of a calcite-filled vein in Wolfcamp shale formation, b) a superposed energy-dispersive x-ray spectroscopy (EDX) map with color-coded elemental abundances; the vein filling mineral is mostly calcite. c) Snapshot of a failed vein in Wolfcamp shale during Brazilian test. Notice the generated debris (black arrow) as a result of the vein failure. For more description, refer to Mighani et al. (2016).

2. EXPERIMENTAL PROCEDURE

Cylindrical samples of Solnhofen limestone were prepared and the end surfaces were ground parallel. The cylinders have a diameter of 38.1 mm and a length between 65.6 and 73.7 mm. Artificial faults with orientations of $\theta = 30$ and 60° (with respect to the sample axis) were then saw-cut and the fault surfaces were finely polished (rms surface roughness= $1.07\ \mu\text{m}$). A gouge mixture was prepared by crushing and sieving the same limestone starting material so that the sample and gouge layer have the same composition. Also, the gouge layer composition is similar to the natural calcite veins such as in Figure 1. The crushed gouge was passed through a $106\ \mu\text{m}$ sieve. Gouge paste was prepared by adding deionized water and was applied as a 1 mm thick gouge layer was placed on the fault surface. A blind borehole with a diameter of 2.92 mm was drilled into the top half of the cylinder. The bottom of borehole in all samples has a constant vertical distance of 6 mm from the fault surface as shown schematically in Figure 2 along with other sample dimensions. The sample was

assembled in a polyurethane jacket as depicted in Figure 2. For a complete description of the experimental procedure refer to Mighani et al. (2018).

Axial stress was measured using load cell outside of the pressure vessel. The axial displacement was measured at the load point (see Figure 2) outside of the pressure vessel using a DCDT displacement transducer. Four piezoelectric transducers recorded the generated acoustic emissions (AE) during the experiments. The piezoelectric ceramics are p-wave type transducers with a resonant frequency of 1.5 MHz. The AE transducers were calibrated with respect to the seismic moment magnitude of ball drop AE events (McLaskey et al., 2015). A vertically oriented strain gauge was also mounted on the bottom half of the sample (foot-wall) below the fault surface to record stress variations adjacent to the fault. A pore pressure transducer outside of the pressure vessel (1.4 kHz frequency response) recorded the pressure variations inside the borehole. A Doppler laser vibrometer with frequency response of 0.5 Hz to 5 MHz measured vertical piston velocity where

axial displacement was controlled (referred to as the load point) outside the pressure vessel. Both axial velocity and displacement (integrated from velocity) were recorded at a 5 MHz sampling rate. The piezoelectric sensors, strain gauge, pore pressure transducer, and laser vibrometer response were recorded using a TraNET EPC-32 acquisition system (Elsys Inc.) with trigger-based sampling rate of 5 MHz. The acquisitions were conducted in a specific mode; after the AE or pore pressure sensor triggers the data record, the data were acquired and streamed to disk with no dead-time which is a major drawback in typical trigger-based acquisition systems; so, it ensures no data loss. In these specific experiments, after the trigger we streamed data for 60 msec at 5 MHz sampling rate. The AE signal was preamplified by 54 dB gain amplifiers; the strain gauge and the pressure transducer signals were input into a signal conditioner (gain $\times 100$ and excitation voltage 2V; frequency response is ~ 140 kHz, limited by the Vishay 2310B signal conditioner) before acquisition. The pore pressure transducer recorded the pore pressure 43.2 cm from the bottom of the borehole through a high-pressure

steel tubing. The laser vibrometer recorded piston motion 40.6 cm from the sample. In order to synchronize these remote measurements with acoustic emissions and stresses from the strain gauge, the pore pressure and vibrometer velocity readings were time-shifted to compensate for the travel times for the compressional waves in the water line and steel axial loading column by 288 and 71 μsec , respectively.

The vibrometer velocity reading is useful in inferring the fault slip velocity and the duration of the stick-slip events (Lockner et al., 2017). The total fault parallel slip can be estimated using two independent ways: 1- integrating the area under the load point velocity record for the slip event duration time ($d = \int v \cdot dt$). 2- provided that the fault slip is large enough to be detected by DCDT, we estimate the fault parallel slip based on the load point axial displacement reading, x_{lp} , (DCDT transducer) and correct for the shortening of the load column (Lockner et al., 2017):

$$d = \frac{x_{lp} - \tau / k_{lp}}{\cos(\theta)} \quad (1)$$

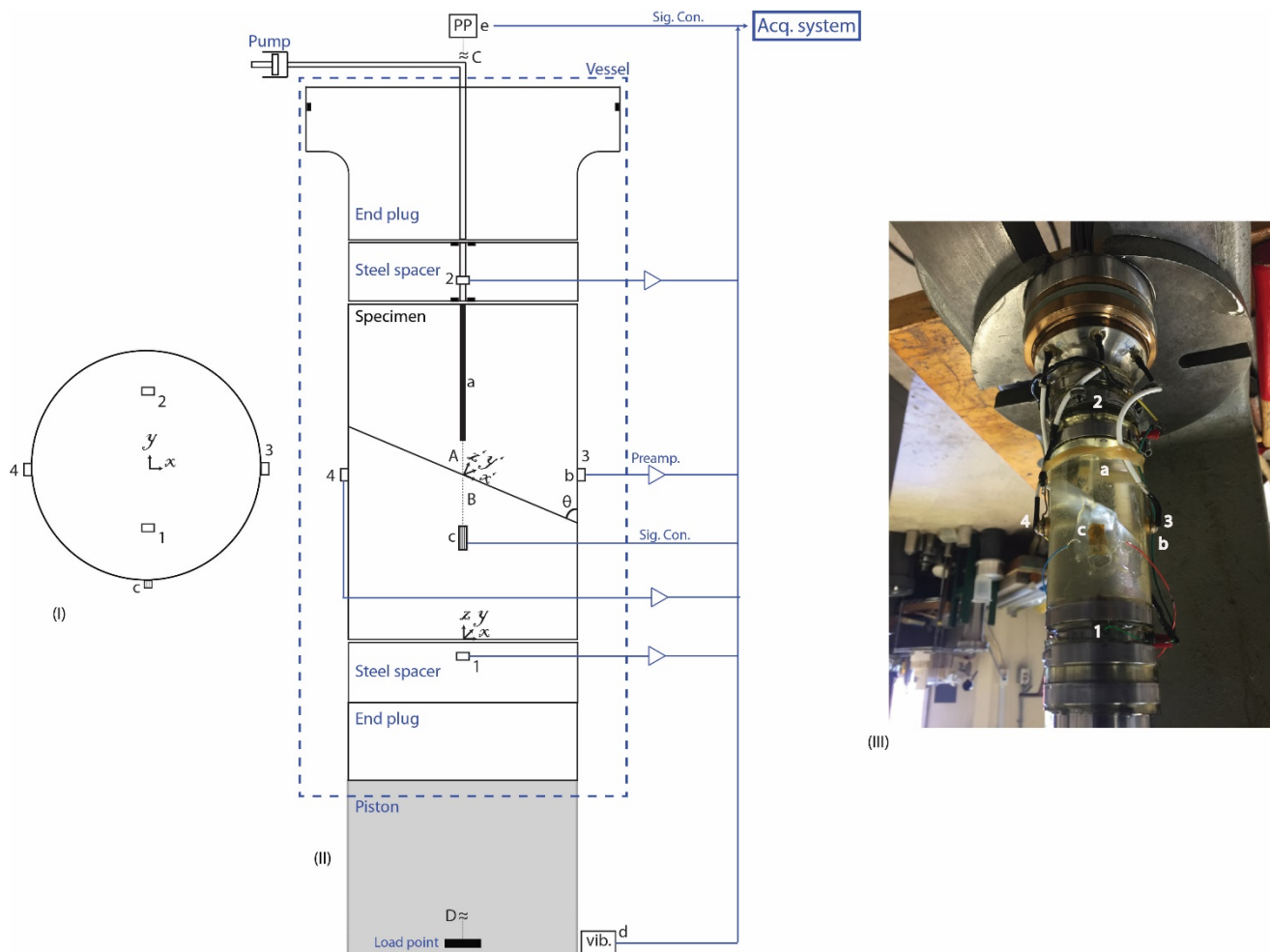


Figure 2. Schematic (I and II) and real picture (III) for the geometry of sample and sensors during the experiments. Note that the schematic is not drawn in scale. (a) is a 2.92 mm diameter blind borehole drilled in the top half of the sample close to a fault with orientation of θ . Two coordinate systems are shown with their origins as xyz and $x'y'z'$; $x'y'z'$ is obtained by clockwise rotation of xyx wrt to y axis by $90-\theta$. (b) is the AE transducer and numbers correspond to the transducer number. (c) is the strain gauge mounted on the sample surface and measuring the stress. (d) is the Doppler laser

vibrometer measuring piston's vertical velocity at the load point. (e) is the pore pressure transducer measuring the borehole pressure. (A) is the vertical distance between borehole bottom and fault which is always 6 mm. (B) is the vertical distance between strain gauge center and fault which is always 15.2 mm. (C) is the distance between pore pressure transducer and borehole bottom which is 43.2 cm. (D) is the distance between load point and sample which is 40.6 cm. The AE signal is fed to a preamplifier, the pore pressure and strain gauge are fed to a signal conditioner. The vibrometer which is calibrated by the provider company has a signal output of mm/s/V. The whole dynamic data is then acquired by the acquisition system.

with τ being the shear stress resolved on the fault plane with orientation θ relative to the vertical axis (see Figure 2). k_{ip} is the system stiffness which is measured to be 49 MPa/mm for the bare surface fault in Solnhofen limestone. For more explanation on the system stiffness refer to Lockner et al. (2017). We determined the system stiffness only for the bare surface fault. The confining pressure in all experiments is maintained at a constant value of 5.0 MPa. Throughout this paper, we use the term “differential stress” which refers to the difference between the maximum (σ_1) and minimum (σ_3) applied stresses. The term “stress drop” is simply the observed drop in the differential stress after an unstable sliding event. We conducted two separate types of experiments. In **sliding experiments**, a constant axial shortening rate of 2 $\mu\text{m}/\text{sec}$ was imposed. In the second type, referred to as **hydraulic fracture**, the axial stress was increased by advancing the piston which was then locked in place when the desired stress was achieved. The pore pressure inside the borehole was then raised by injecting deionized water under a constant injection rate of 2.6 cm^3/min . After a critical pore pressure, i.e. breakdown pressure (BP), the hydraulic fracture initiated and propagated towards the fault.

3. OBSERVATIONS

3.1. Sliding Experiments

The fault surfaces were sheared briefly with an axial shortening rate of 2 $\mu\text{m}/\text{sec}$ before each hydraulic fracture experiment. The bare fault surfaces were slid for less than 0.2 mm axial shortening to maintain the original polished surface and avoid formation of surface wear grooves.

Table 1. Frictional properties of the faults during sliding experiments. μ in bare and gouge-filled surfaces is reported at 0.2 mm and 1 mm fault parallel slip, respectively. SH and number in names stand for Solnhofen and fault orientation, respectively.

Experiment Name	μ
SH30-Bare	0.12
SH60-Bare	0.11
SH30-Gouge	0.65
SH60-Gouge	0.42

The gouge-filled faults were sheared for 1 mm axial shortening to pre-condition the gouge and fault surface. The reported coefficient of friction is summarized in Table 1. Figure 3 shows the evolution of μ during the

sliding experiments. The 1mm thick gouge layer is significantly stronger ($\mu \geq 0.42$). For the gouge-filled surfaces, μ is notably lower for the 60° fault than for the 30° fault. It also runs at a slightly lower μ in 60° fault compared to the 30° fault in the bare surface sliding tests. Lower μ at less oblique fault angles has been previously observed in granite (Savage et al., 1995) and in Solnhofen limestone (Donath et al., 1972). The unstable (stick-slip) sliding experiments in PMMA by Mighani et al. (2018) also showed lower μ for a 60° fault compared with a 30° fault. One more notable difference between the two surfaces is the strain-hardening behavior; the gouge-filled surface still experiences strain-hardening after 1 mm displacement, while the bare surface has a comparatively flat frictional behavior at 0.2 mm displacement. During this initial stage in both bare and gouge-filled faults, only stable sliding was observed.

3.2. Hydraulic Fracture Experiments

The hydraulic fracture was generated after pressurization of the borehole fluid. In this section, we present results for four HF experiments conducted on samples with bare surface and gouge-filled faults. The experimental conditions and the results are summarized in Table 2. The differential stress for the bare surface tests is 1 MPa. Due to low frictional strength, higher differential stresses were not possible for HF tests with bare surface fault. The differential stress value for gouge tests was the value at the end of 1 mm axial shortening.

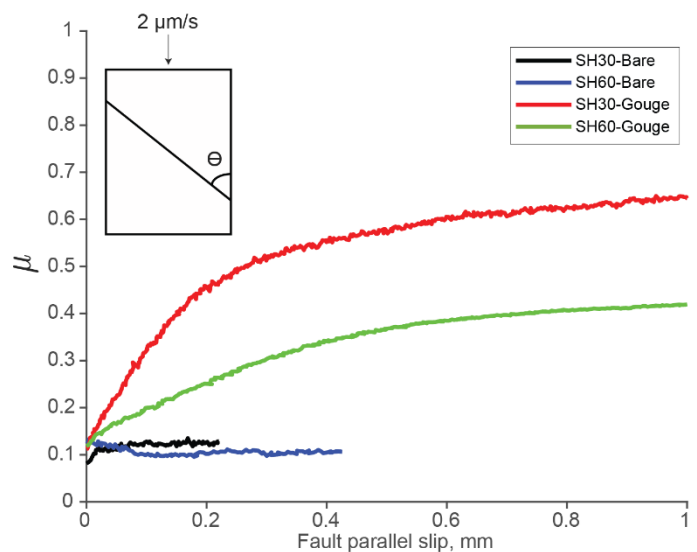


Figure 3. The evolution of the coefficient of friction, μ , during sliding experiments in bare and gouge-filled Solnhofen limestone fault surfaces. The x axis is the fault parallel slip derived by subtracting the piston elastic

shortening from the axial displacement (see main text). The gouge is a 1 mm thick layer of Solnhofen powder with < 106 μm grain size. Notice the increased μ value in gouge-filled surfaces. SH60-Gouge shows a strong strain-hardening which might reach closer to the SH30-Gouge curve at longer slip displacements; however, for the reasons explained in the text we did not slip the faults further to explore this.

In order to avoid disturbance of the evolved sheared gouge, we chose not to modify this value by adjusting

Table 2. Experimental conditions for hydraulic fracture experiments. The experiment's name is adapted as material (SH for Solnhofen)-fault angle (degrees)-B as bare surface or G as gouge-differential stress (MPa). DS: Differential stress prior to HF. BP: Breakdown pressure. SD, Stress drop. Inferred slip is estimated from the vibrometer velocity readings. DCDT slip is estimated by correcting the DCDT data for piston elastic shortening. Fluid diffusion time is discussed in section 4 and Figure 6.

Experiment Name	DS, MPa	BP, MPa	Inferred maximum slip velocity, mm/s	Slip duration, μs	Inferred slip, μm	DCDT Slip, μm	Fluid Diffusion time, msec	SD, MPa	SD, %	Interaction
SH30-B-1	1	39	0.5	29.9	0.01	-	1.42	0.5	50	Cross
SH60-B-1	1	28	0.3	37.4	0.02	-	4.09	0	0	Arrest
SH30-G-12	12	23	2.9	2533.8	2.48	59	4.18	6.4	53	Arrest
SH60-G-20	20	24	8.2	3406.5	19.04	331	4.31	18.8	94	Arrest

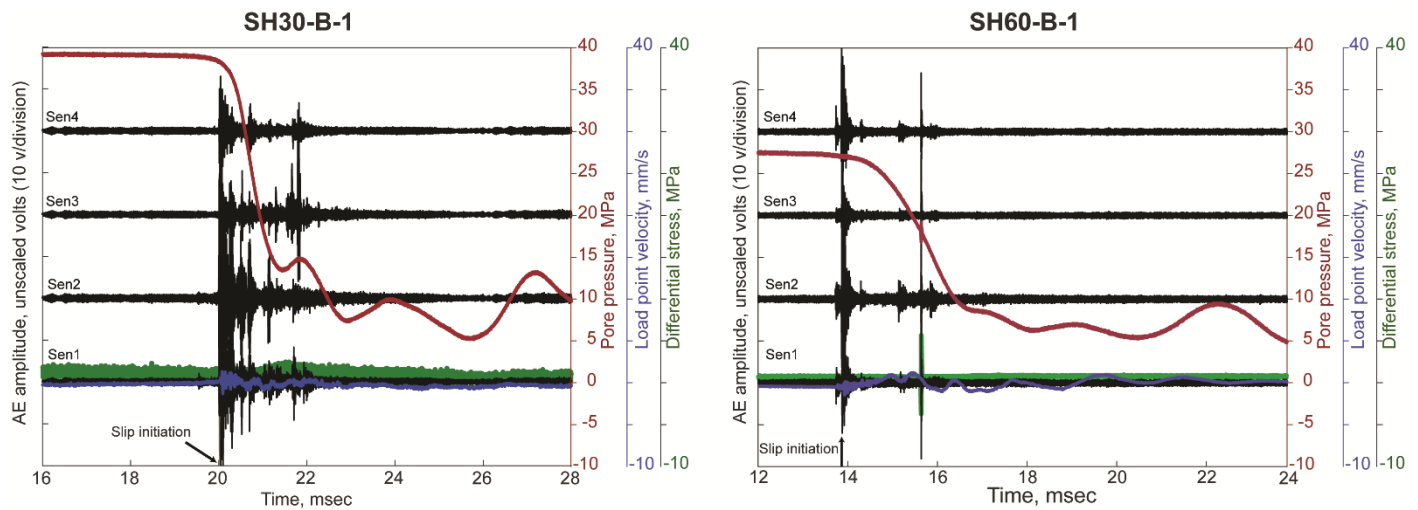


Figure 4. The recording of hydraulic fracture experiments for bare surface fault tests in Solnhofen limestone with 30⁰ (left) and 60⁰ (right) orientations. The hydraulic fracture was able to cross the fault at 30⁰ orientation. Notice the short fault slip durations in vibrometer readings compared to Figure 5. The signal burst at ~ 15.8 msec in SH60-B-1 test is due to an unknown electrical noise (~120 Hz) source. The unscaled AE amplitudes have been calibrated based on ball drop experiments and the calibrated AE moment of the slip events are shown in Figure 7. The time of slip initiation is indicated based on the burst in AE signals.

the piston prior to HF tests. Therefore, the differential stress in gouge-filled 30⁰ and 60⁰ faults was 12 and 20 MPa, respectively, after 1 mm sliding and prior to HF experiments. Although it would have been better to keep the differential stresses the same in all HF experiments, but it was not possible due to the mentioned constraints for both bare and gouge-filled faults. Figure 4 shows the HF results for bare surface.

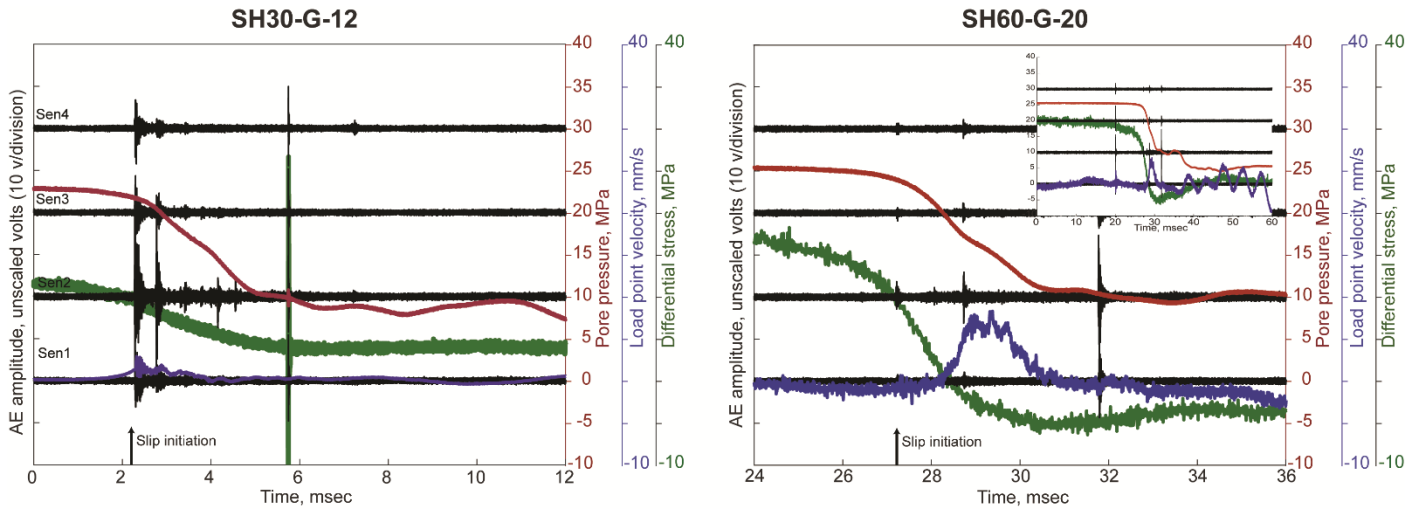


Figure 5. The recording of hydraulic fracture experiments for gouge-filled fault tests in Solnhofen limestone with 30° (left) and 60° (right) orientations. There is a large stress drop in both experiments, while the AE signals are less noisy compared with bare surface fault tests (Figure 4). The vibrometer also records a long duration slip event. We also show the entire recording in the right figure which shows the recovered stress level after a transient weakening. The signal burst at ~ 5.8 msec in SH30-G-12 test is due to an unknown electrical noise (~ 120 Hz) source. The unscaled AE amplitudes have been calibrated based on ball drop experiments and the calibrated AE moment of the slip events are shown in Figure 7. The time of slip initiation is indicated based on the burst in AE signals.

Based on the high rate recorded response (Figures 4 and 5), there are some notable characteristics during the HF intersection. The slip on the fault can be detected independently by vibrometer, strain gauge, and acoustic emission signals. It results in an abrupt change in the vibrometer velocity, significant generated acoustic signal, and a partial stress drop. The abrupt pore pressure drop is associated with the slip on the fault. The pore pressure then drops to the confining pressure value as the pore fluid reaches the sample jacket. We determined the time of slip initiation based on the burst in AE signals. The AE-based slip initiation coincides with the vibrometer velocity increase. The strain gauge readings, especially in the gouge experiments with high differential stress tend to decrease before the slip starts. This decrease could be related to the Poisson's effect during the fluid injection into the borehole. As the fluid is injected into the borehole, the sample expands radially and because of the Poisson's effect it becomes shorter. Since the piston is locked, the vertical stress tends to decrease which can be seen in Figure 5.

The HF was able to cross the bare surface fault to the other side of the fault at fault orientations of 30° , and 45° (see Mighani et al., 2018 for 45° fault results), but not at 60° . The intersection of the HF and fault is associated with an AE signal burst, pore pressure drop, slip velocity increase, and stress drop (see Figure 4). The stress drop was less than 0.5 MPa and the slip duration was short, on the order of ~ 30 μ sec. The maximum inferred slip velocity did not exceed 0.5 mm/sec.

The HF was arrested by the gouge-filled fault for fault orientations of 30° and 60° . In contrast to the bare surface fault, the slip was associated with a large stress

drop and the AE bursts during the fault slip were less noisy (see Figure 5). The slip duration was ~ 2.5 - 3.5 msec and the maximum inferred slip velocity reached ~ 3 - 8 mm/sec (see Table 2). The slip values in Table 2 were estimated using two independent methods (see section 2). Note that the slip values obtained from DCDT are much larger than the inferred slip by the vibrometer. This might be due to the fact that the inferred slip velocity considers only the slip duration time window; while, DCDT measures an accumulated displacement over 1 second (DCDT sampling rate is 1 Hz). Nevertheless, the relative total slip between 30° and 60° gouge-filled fault remains roughly the same. In the following section, we examine the distinctions between the bare surface and the gouge-filled fault behavior during the HF intersection.

4. SLOW SLIP ON THE GOUGE-FILLED FAULT

In order to better compare the inferred slip velocity and pore pressure response during these tests, they are shown separately in Figure 6. After the HF intersects the fault, the pore pressure declines until the fluid front reaches the jacket. After reaching the jacket it is associated with a back-pressure which results in a jump in the pressure response. We can then determine the fluid travel time to reach the fault boundary from this pressure spike. The pore pressure finally declines to the confining pressure value. Comparing the slip duration time with fluid diffusion time (Table 2) in bare surface fault tests suggests that the fluid front traveled with much slower rates than the slip pulse (2 orders of magnitude difference in the two time constants). On the other hand,

the fluid diffusion time and the slip duration for the gouge-filled tests are roughly equal, within the same order of magnitude. Although it is possible for the pressure spikes to be related to the pore fluid system's (pore pressure transducer + pore fluid lines + borehole fluid...) ringing during the pressure drop, we have evaluated the pore pressure response to a step-wise pressure drop during a burst disk failure. Appendix B describes these tests. The rise time in the pore pressure response to this step function was 603-705 μ s, equivalent to 1.4-1.7 kHz frequency response. Therefore, any rise time longer than this value, i.e. the case of all our HF experiments, seems physically meaningful.

The AE and stress drops can easily be evaluated by comparing Figures 4 and 5. The large fault displacements and stress drops after the HF intersection did not reflect into the radiated stress waves or AE response. In other words, in contrast to the bare surface fault, the slip on the gouge-filled fault occurred with much less radiated AE events. This suggests that relying merely on the high frequency AE events to interpret the sliding behavior may be misleading, especially when the fault slides on the fault gouge.

Having the gouge grains changes both the mechanical interaction of the fault surfaces and the accessible volume for fluid flow inside the fault. The sliding experiments in the presence of glass beads or angular quartz grains (Mair et al., 2002) and their numerical simulations (Morgan and Boettcher, 1999; Morgan, 2004) suggest the dominant role of "Particle rolling" in the case of spherical grains and "inter-particle sliding" and "dilation" in the case of angular grains during the sliding of a gouge-filled fault. The role of fault gouge in stabilizing the sliding has also been experimentally observed in the literature. The granite sliding experiments by Byerlee and Summers (1976) suggest that the presence of fault gouge shifted the stable to unstable normal stress transition to higher values of normal stress. This effect was enhanced by increasing the gouge thickness. In experiments by Engelder (1973), the stick-slip sliding in bare surface Tennessee sandstone became stable when the fault gouge was inserted between the fault surfaces. The dilatancy hardening which modifies the local effective stress on the fracture tip may also explain some of the observations. Triaxial experiments by French and Zhu (2017) suggest that under similar nominal effective stresses, at elevated fluid pressures, the dilatancy hardening results in lengthened duration of failure. So, the failure rate is limited by the ability of the fluid to fill the void volume and reach the newly formed fracture tip. This may explain why in gouge-filled fault tests, the fluid and slip front coincided (fluid diffusion time roughly equal to slip duration).

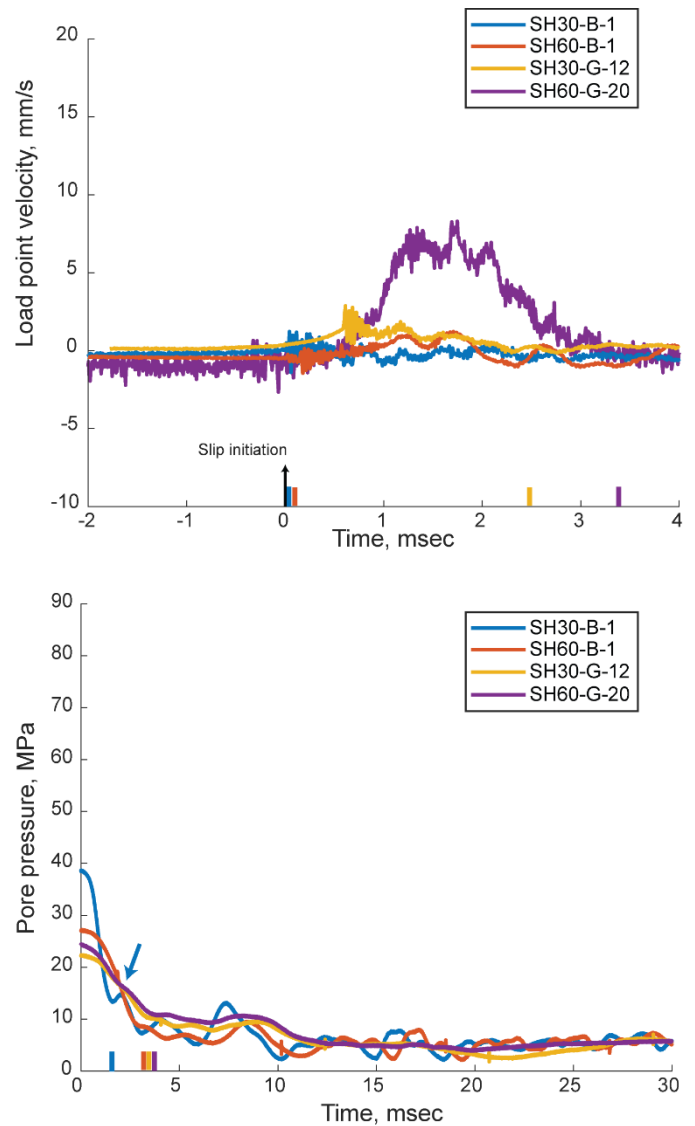


Figure 6. Slip velocity response (top) and pore pressure (bottom) comparison for bare surface and gouge-filled fault surfaces. In the top figure, the slip duration is indicated on the x axis using vertical lines. In the bottom figure, the timing of the fluid front reaching the fault boundary (fluid diffusion time) is determined on the x axis from the pressure spikes (e.g. blue arrow in the bottom figure for SH30-B-1). Notice the long duration of slip and smeared pore pressure decline in the gouge-filled tests. For description of test names refer to Table 2. Note that compared to Figures 4 and 5, the sensors response in this figure are time-shifted so that slip (top) and pore pressure decline (bottom) initiate at time zero.

In total, the presence of the fault gouge resulted in a distinctly different activation of the fault when compared to the bare surface fault. Characteristics were manifested as: 1- The slip velocity readings from the vibrometer recorded longer duration slip events for the gouge-filled faults (see Figure 6). 2- The piezoelectric transducers recorded AE events with lower amplitude for the gouge-filled fault (see Figures 4 and 5). 3- The stress drop was greater in the gouge-filled fault with a long weakening time and greater weakening (see Figures 4 and 5). 4- The

transient pore pressure decline response was longer in the gouge-filled fault with lower back-pressure spikes (smeared fluid diffusion) (see Figure 6). These observations suggest that the fault gouge promotes longer duration slower slip events.

5. SLIP SOURCE ANALYSIS

The seismic moment magnitude of the AE events was estimated using a ball drop experiment which is explained in Appendix A. The ball drop experiments are helpful for both obtaining the moment magnitude and estimating the instrument response during AE recording. The time window for deriving the signal spectrum is selected so that the entire event is captured. Based on trial in these slip events, a 400 μ sec time window is long enough to represent the event with the middle of the time window at the signal peak amplitude. Notice that the time window does contain a cluster of AE events, not just a single event. So, the seismic spectrums and estimated moments are for the cluster of AE events during the slip. Figure 7 shows the spectrum of the slip events in different tests after removing the instrument response from the raw signal recordings. The seismic moment and the equivalent moment magnitude of the AE events shown in Figure 7 were estimated using ball drop experiments. The slip events in these experiments are similar to stick-slip events in the sense that the slip ruptures the entire fault surface. Since the slip event is not contained within the rock, the source dimension analysis becomes more complicated (Thompson et al., 2009). Therefore, the formulations for contained events such as the Brune type shear event (Brune, 1970) were not relevant for these events. Consequently, we were not able to invert for source dimension in these events.

The released quasi-static moment during the fault's sliding can be estimated by using the following equation (McGarr, 2012):

$$M_{QS} = GAD \quad (2)$$

with G being the medium shear modulus, A , the rupture area, and D the fault parallel displacement. In these experiments, Solnhofen limestone's shear modulus is ~ 16 GPa. The rupture area for these slips events, A , is the entire fault surface as discussed. D is the fault parallel displacement shown in Table 2. When the DCDT slip displacements were below the resolution, we used the vibrometer inferred slip values. The vibrometer inferred slip tends to be on the lower end as the comparison between the two slip values in the gouge experiments indicate. Therefore, the vibrometer inferred slip gives a lower bound on the released moment. Notice that in this form of equation, the unloading stiffness which is a lumped function of the sample and loading frame stiffness contribute to D ; the higher the stiffness, the lower D and as a result the lower M_{QS} will be

(McGarr, 2012: eqs. 5 and 7). The seismic and quasi-static moments are summarized in Table 3.

Table 3. Results of source analysis during the faults slip after hydraulic fracture intersection. The second and third columns are the estimated seismic source moment and moment magnitude, respectively. The fourth column is the estimated released quasi-static moment.

Experiment Name	M_0 , N.m	M	M_{QS} , N.m
SH30-B-1	22	-5.17	> 4*
SH60-B-1	20	-5.20	> 4*
SH30-G-12	12	-5.33	2077
SH60-G-20	1	-5.97	6884

*Based on the vibrometer inferred slip

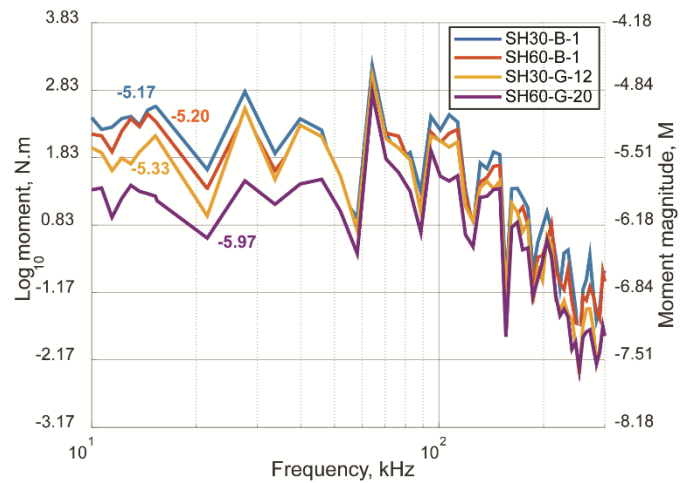


Figure 7. Spectrum of AE events during slip events after HF intersection with the fault. The instrument response is removed from the raw signals and the response is calibrated based on ball drop experiments. The numbers on the curves correspond to the equivalent moment magnitude of the AE events (see Table 3)

Table 3 suggests that even though the released moment during the fault gouge sliding is three orders of magnitude higher than the bare surface tests, the released seismic moment in the gouge experiments is lower. This suggests that the seismic efficiency in the gouge-filled experiments is orders of magnitude lower than the bare surface experiments. It reaffirms the slow slip failure mechanism for gouge experiments, as discussed in section 4.

6. SIMILARITY TO LPLD EVENTS

During the microseismic recordings of hydraulic fracture operations in clay-rich Barnett shale, Das and Zoback (2011) observed some Long Period Long Duration (LPLD) events in association with the microseismic events. The LPLD events had a duration of 10-100 sec in contrast to the usual ~ 0.1 s long microseisms. These events were in the 10-80 Hz frequency band compared

with ~ 1 kHz microseisms. Zoback et al. (2012) suggested that the LPLDs occur as a result of the sliding on the natural fractures which do not have a favorable orientation for sliding under *in-situ* stresses. Therefore, under high fluid pressure they can activate, but the slip does not go unstable (due to the fault orientation). Therefore, the rupture front does not exceed the fluid front. The experiments in this report suggested an additional mechanism for the generated slow slip events during the sliding of the natural faults. As described in sections 4 and 5, the fault gouge has developed small AEs, long duration slip events compared with a bare surface fault. The relative sliding of the fault surfaces can be accommodated by relative displacement and rotation of the fault gouge grains. Figure 8 shows a schematic of this sliding in the presence of the fault gouge grains. Therefore, sliding occurs under slow slip resulting in a significant displacement (slip) on the fault (see Table 2). So, the presence of gouge grains can stabilize the fault more towards a slower slip with less generated acoustic waves or AEs, similar to the low frequency LPLD events.

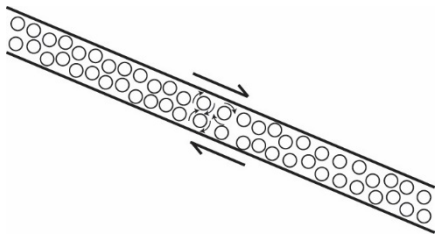


Figure 8. The schematic for the slip on a gouge-filled fault. The grains during the sliding can rotate and displace to facilitate the displacement along the fault.

7. CONCLUSIONS

We conducted hydraulic fracture experiments in Solnhofen limestone and in the presence of a pre-loaded fault. The fault was either bare surface or contained 1 mm thick fault gouge layer. The hydraulic fracture was not able to cross the gouge-filled fault. Instead, it generated a significant stress drop due to the induced fault slip. A characteristic slip event was detected by the laser vibrometer for the gouge-filled fault tests; the slip had a longer duration but with similar slip velocity as the bare surface fault. Therefore, the total fault slip increased. The increased total slip and stress drop in the gouge-filled fault occurred while the AE slip events were lower magnitude in the gouge-filled fault. In other words, the released quasi-static moment was larger for gouge-filled faults, while the seismic efficiency was lower. The slip duration for the bare surface fault tests is 2 orders of magnitude faster than the fluid diffusion time; so the fluid front lags behind the slip front. While, for gouge-filled fault tests, these two values are within the same order, i.e. the slip front does not exceed the fluid front. The observed gouge events are similar to the stable LPLD events observed by Zoback et al. (2012)

during the activation of stimulated natural fractures in Barnett shale. The resulting slow slip could be effective in generating a connected fracture network which may not be detected as acoustic emissions/seismic signals.

Acknowledgments. SM's and BE's contribution was supported by the U.S. Department of Energy, Office of Science, Office of Basic Energy Sciences, Chemical Sciences, Geosciences, and Biosciences Division under Award Number DE-FG0109ER14760. We would thank Arthur McGarr and Nick M. Beeler for their constructive reviews. We would also like to acknowledge B. Proctor for help with the experiments and Y. Bernabe for thoughtful comments that greatly improved this work. Any use of trade name, firm, or product name is for descriptive purposes and does not imply endorsement by MIT nor the U.S. Government. Data used to generate the figures seen in this report can be found at <https://doi.org/10.5066/F7SN0886>. Or you could say. Data used to generate the figures seen in this report are in Saied et al. (2018).

REFERENCES

1. Blanton, T.L. 1982. January. An experimental study of interaction between hydraulically induced and pre-existing fractures. In SPE unconventional gas recovery symposium. Society of Petroleum Engineers.
2. Blanton, T.L. 1986. January. Propagation of hydraulically and dynamically induced fractures in naturally fractured reservoirs. In SPE unconventional gas technology symposium. Society of Petroleum Engineers.
3. Bungler, A.P., Kear, J., Jeffrey, R.G., Prioul, R. and Chuprakov, D. 2015. Laboratory investigation of hydraulic fracture growth through weak discontinuities with active ultrasound monitoring. In 13th ISRM International Congress of Rock Mechanics. International Society for Rock Mechanics.
4. Brune, J.N. 1970. Tectonic stress and the spectra of seismic shear waves from earthquakes. *Journal of geophysical research*, 75(26), pp.4997-5009.
5. Byerlee, J. and Summers, R. 1976. A note on the effect of fault gouge thickness on fault stability. In *International Journal of Rock Mechanics and Mining Sciences & Geomechanics Abstracts* (Vol. 13, No. 1, pp. 35-36). Pergamon.
6. Das, I. and Zoback, M.D. 2011. Long-period, long-duration seismic events during hydraulic fracture stimulation of a shale gas reservoir. *The Leading Edge*, 30(7), pp.778-786.
7. Engelder J. T. 1973. Quartz fault-gouge, its generation and effect on the frictional properties of Sandstone, (Ph.D. dissertation). College Station. Texas A&M University, p. 154.
8. French, M.E. and Zhu, W. 2017. Slow fault propagation in serpentinite under conditions of high pore fluid pressure. *Earth and Planetary Science Letters*, 473, pp.131-140.
9. Gale, J.F., Reed, R.M. and Holder, J. 2007. Natural fractures in the Barnett Shale and their importance for hydraulic fracture treatments. *AAPG bulletin*, 91(4), pp.603-622.

10. Hanson, M.E., Anderson, G.D. and Shaffer, R.J. 1980. Theoretical and experimental research on hydraulic fracturing. *J Energy Resour Technol Trans ASME*, 102(2), pp.92-8.
11. Gu, H., Weng, X., Lund, J.B., Mack, M.G., Ganguly, U. and Suarez-Rivera, R. 2012. Hydraulic fracture crossing natural fracture at nonorthogonal angles: a criterion and its validation. *SPE Production & Operations*, 27(01), pp.20-26.
12. Hanks, T.C., and H. Kanamori. 1979. A moment magnitude scale, *J. Geophys. Res.* 84, 2348–2350.
13. Lockner, D.A., Kilgore, B.D., Beeler, N.M. and Moore, D.E. 2017. The Transition from Frictional Sliding to Shear Melting in Laboratory Stick-Slip Experiments. *Fault Zone Dynamic Processes: Evolution of Fault Properties During Seismic Rupture*, 227, p.105.
14. Mair, K., Frye, K.M. and Marone, C., 2002. Influence of grain characteristics on the friction of granular shear zones. *Journal of Geophysical Research: Solid Earth*, 107(B10).
15. Mayerhofer, M.J., Lolon, E., Warpinski, N.R., Cipolla, C.L., Walser, D.W. and Rightmire, C.M. 2010. What is stimulated reservoir volume?. *SPE Production & Operations*, 25(01), pp.89-98.
16. McGarr, A. 2012. Relating stick-slip friction experiments to earthquake source parameters, *Geophys. Res. Lett.*, 39, L05303.
17. McLaskey, G.C., Lockner, D.A., Kilgore, B.D. and Beeler, N.M. 2015. A robust calibration technique for acoustic emission systems based on momentum transfer from a ball drop. *Bulletin of the Seismological Society of America*, 105(1), pp.257-271.
18. Mighani, S., Taneja, S., Sondergeld, C.H. and Rai, C.S., 2015, November. Nanoindentation creep measurements on shale. In 49th US Rock Mechanics/Geomechanics Symposium. American Rock Mechanics Association.
19. Mighani, S., Sondergeld, C.H. and Rai, C.S. 2016. Observations of tensile fracturing of anisotropic rocks. *SPE Journal*, 21(04), pp.1-289.
20. Mighani, S., Lockner, D. A., Kilgore, B. D. and Evans, B. 2018. Interaction Between Hydraulic Fracture and a Preexisting Fracture under Triaxial Stress Conditions. SPE paper 189901-MS presented at the 2018 Hydraulic Fracturing Technology Conference.
21. Morgan, J.K. 2004. Particle dynamics simulations of rate-and state-dependent frictional sliding of granular fault gouge. *Pure and Applied geophysics*, 161(9-10), pp.1877-1891.
22. Morgan, J. K. and Boettcher, M. S. 1999. Numerical Simulations of Granular Shear Zones Using the Distinct Element Method: II Effects of Particle Size Distribution and Interparticle Friction on Mechanical Behavior, *J. Geophys. Res.* 104, 2721–2732.
23. Savage, J.C., Lockner, D.A. and Byerlee, J.D. 1996. Failure in laboratory fault models in triaxial tests. *Journal of Geophysical Research: Solid Earth*, 101(B10), pp.22215-22224.
24. Thompson, B.D., Young, R.P. and Lockner, D.A. 2009. Premonitory acoustic emissions and stick-slip in natural and smooth faulted Westerly granite. *Journal of Geophysical Research: Solid Earth*, 114(B2).
25. Tinni, A., Fathi, E., Agarwal, R., Sondergeld, C.H., Akkutlu, I.Y. and Rai, C.S. 2012. Shale permeability measurements on plugs and crushed samples. In SPE Canadian Unconventional Resources Conference. Society of Petroleum Engineers.
26. Warpinski, N.R. and Teufel, L.W. 1987. Influence of geologic discontinuities on hydraulic fracture propagation (includes associated papers 17011 and 17074). *Journal of Petroleum Technology*, 39(02), pp.209-220.
27. Zoback, M.D., Kohli, A., Das, I. and McClure, M.W. 2012. The importance of slow slip on faults during hydraulic fracturing stimulation of shale gas reservoirs. In SPE Americas Unconventional Resources Conference. Society of Petroleum Engineers.
28. Mighani, S., Lockner, D.A., Kilgore, B.D., and Evans, B., 2018, Data release for "Role of Fault Gouge during Interaction between Hydraulic Fracture and a Preexisting Fracture": U.S. Geological Survey data release, <https://doi.org/10.5066/F7SN0886>.

APPENDIX A

Following McLaskey et al. (2015), we calibrated the AE transducers response using ball drop experiments. Note that the notations in this section are similar to McLaskey et al. (2015), but not necessarily the same. The subscript “int” refers to an AE source and “ext” refers to a ball drop source. The main motivation behind AE calibrations was to decompose the instrument-apparatus response from the recorded signal and estimate the seismic moment magnitude of the AE events. This way, we use an external source (ball drop) to calibrate the internal sources (AEs). A steel ball with a diameter of 6.3 mm and mass of $m=1.02$ g was dropped from a height of 17.8 cm onto the center of sample’s top surface. These experiments are conducted on bench-top while we applied a vacuum to the jacketed sample to ensure a good sample/sensor coupling. The vacuum acts as if the sample was instead confined to a confining pressure of 1 bar. We recorded the generated AE and the timespan between the ball’s first and second impact. We infer the first impact velocity from $v_1 = \sqrt{2h/g}$ with h and g being the free-fall drop height and the Earth’s gravitational acceleration, respectively. The time difference between the first and the second impact, Δt , helps compute the rebound velocity as $v_2 = \sqrt{g \cdot \Delta t / 2}$. The change of momentum is then calculated as $\Delta P = m(v_2 - v_1)$ where v_i is a vector. The theoretical impact source spectrum is then obtained from the spectrum of the theoretical force-time function normalized by the change of momentum. The instrument-apparatus response spectrum, Ψ_{ext} , was then derived by dividing the measured signal by the theoretical spectrum. The spectrums are shown in Figure A1 for Solnhofen limestone. The preamplifier is equipped with a 10 kHz high-pass filter. Therefore, the

observed and theoretical ball drop impulse signals are shown at frequency lower bound of 10 kHz.

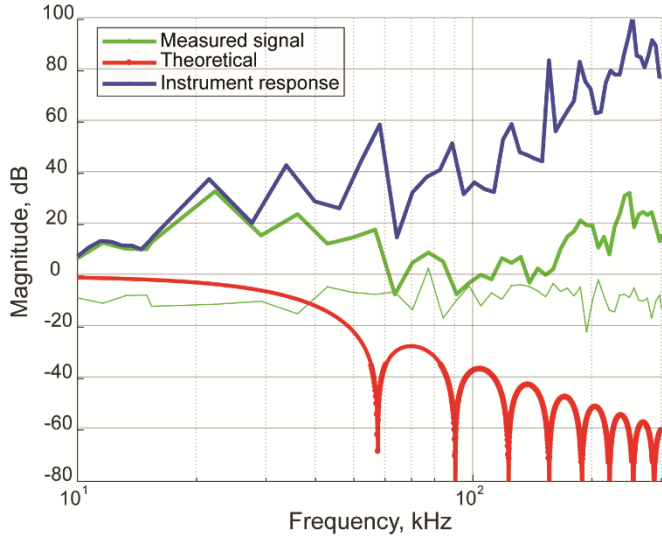


Figure A1. Calibration of AE sensors response for their magnitude based on the ball drop experiments for Solnhofen limestone. The red line is the spectrum of the theoretical ball drop response, the green line is the measured AE signal in the lab. The AE signal spectrum is obtained from a time window of ~2 ms including the event. The blue line is the instrument response obtained by dividing the measured signal by the theoretical spectrum. Note that the y axis is in dB units (logarithmic) and dividing between the two responses is simply done by subtracting the two responses. The thin green line also shows the background noise spectrum. Notice the good signal-to-noise ratio for a wide frequency band. Local peaks observed in the signal spectrum coincide with the noise spectrum.

The corner frequency in the ball drop experiment for Solnhofen limestone is 34 kHz. The observed and theoretical ball drop spectrums in Figure A1 have the same corner frequency. The change of momentum (ΔP) in the ball drop experiments is 0.0035 N.s. The observed Δt in ball drop experiments is 301 msec. For internal AE sources, the instrument response, Ψ_{int} , is obtained from the observed AE signal, i.e. S_{int} (McLaskey et al., 2015):

$$\Psi_{ext} = C_{FM} \cdot \Psi_{int} \quad (A1)$$

C_{FM} is the force-moment-rate constant which is equal to $(V_p + V_s)$ with V_p and V_s being the material's compressional and shear velocity, respectively. C_{FM} for Solnhofen limestone is 8.9 km/sec. For an AE source:

$$S_{int} = M_0 \cdot \Psi_{int} \quad (A2)$$

Now, combining eq. A1 and A2 we can obtain the moment of the internal AE events as:

$$M_0 = \Delta P \times C_{FM} / (\Psi_{ext} / S_{int}) \quad (A3)$$

And the equivalent moment magnitude is (Hanks and Kanamori, 1979):

$$M = 2/3 \times \log_{10}(M_0) - 6.067 \quad (A4)$$

The equivalent moment magnitude for ball drop experiments in the limestone is -5.04.

APPENDIX B

The pore pressure transducer is a Honeywell Inc. Ultra Precision Super TJE model. The manufacturer stated frequency response is 2 kHz. In order to evaluate the frequency response of the pore fluid pressurizing system, the sample assembly was replaced with a fragile disk. This burst disk fails rapidly at a nominal pressure of 15 MPa. We recorded this burst-type pressure release event using the same recording system and procedure as the HF events at an acquisition rate of 5 MHz. Figure B1 shows the transducer response for this burst event in three separate tests. For the first experiment, a long pipe was attached before the disk. The pipe had the same length as the sample assembly line. Water was added to a closed chamber behind the disk, so it burst into a small fluid reservoir, roughly similar to a real HF experiment. For the second experiment, the small fluid reservoir was removed and the disk burst into air. In the third case, the long pipeline was removed and the disk was still open to air. As can be observed in Figure B1, the abrupt burst event produced a characteristic transducer response with a certain rise time. This rise time is related to the transducer's frequency response. For instance, the rise time of 705 μ sec in Figure B1 corresponds to a frequency response of 1.4 kHz. Therefore, the transducer acts as a low-pass filter and the recorded signal is physically meaningful for frequencies up to 1.4 kHz. The frequency spectrum analysis of the response also shows a flat response up to a corner frequency of 1.4 kHz. The response rolls off abruptly above this corner frequency.

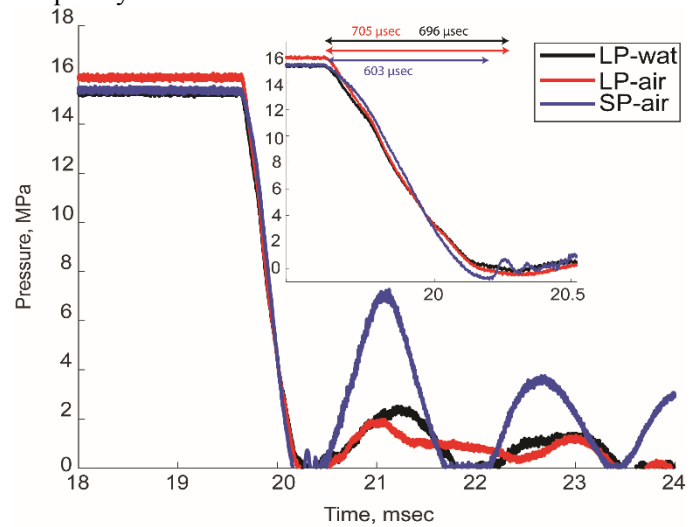


Figure B1. The pore pressure response for three burst disk tests as explained in the text. The transducer records this instantaneous pressure drop with a rise time between 603-705 μ sec, equivalent to frequency response of ~1.4-1.7 kHz. SP and LP stand for short pipe and long pipe. Wat stands

for water. For an explanation of these three experiments refer to the text in Appendix B.